Journal of Power Sources 208 (2012) 225–231

Contents lists available at SciVerse ScienceDirect

Journal of Power Sources

journal homepage: www.elsevier.com/locate/jpowsour

Enhanced ionic conductivity of $Ce_{0.8}Sm_{0.2}O_{2-\delta}$ by Sr addition

Zhan Gao[a,*], Xingmin Liu[b], Bill Bergman[a], Zhe Zhao[a,b,*]

[a] Division of Ceramic Technology, Department of Materials Science and Engineering, KTH Royal Institute of Technology, SE-10044 Stockholm, Sweden
[b] Department of Materials and Environmental Chemistry, Arrhenius Laboratory, Stockholm University, SE-10691 Stockholm, Sweden

ARTICLE INFO

Article history:
Received 26 July 2011
Received in revised form 3 November 2011
Accepted 1 January 2012
Available online 4 February 2012

Keywords:
Solid oxide fuel cells
Electrolyte
Co-doped
Ceria
Conductivity
Grain-boundary conductivity

ABSTRACT

Sm and Sr co-doped ceria-based electrolyte with compositions of $Ce_{0.8}(Sm_{1-x}Sr_x)_{0.2}O_{2-\delta}$ ($x = 0, 0.3, 0.5, 0.7$) are synthesized and investigated with the aim of improving the electrical properties of $Ce_{0.8}Sm_{0.2}O_{2-\delta}$. X-ray diffraction (XRD) and electron microscope (SEM and TEM) techniques are employed to characterize the microstructure of powders and sintered pellets. The ionic conductivity has been examined by the A.C. impedance spectroscopy in air. The $Ce_{0.8}(Sm_{0.7}Sr_{0.3})_{0.2}O_{2-\delta}$ exhibits the highest bulk conductivity among the series, which can be mainly ascribed to the increase of oxygen vacancy concentration. The specific grain-boundary conductivities are observed to increase with the Sr doping content up to $x = 0.5$. Further increase in Sr concentration will lead to reduced specific grain-boundary conductivities. The total conductivities of all Sm and Sr co-doped ceria are higher than that of $Ce_{0.8}Sm_{0.2}O_{1.9}$. The results indicate that Sr co-doping opens a new avenue to improve ionic conductivity in $Ce_{0.8}Sm_{0.2}O_{1.9}$.

1. Introduction

Solid oxide fuel cells (SOFCs) are energy generation devices electrochemically convert chemical energy to electrical energy characterized by high efficiency and environmentally friendly. Traditional SOFCs based on yttria stabilized zirconia (YSZ) electrolyte are usually operated in the high-temperature range (800–1000 °C) to reach the required conductivity and high power output. However, high-temperature operation causes difficulty in material selection and sealing, which blocks the commercial process of the SOFCs. Alternatively, the low to intermediate-temperature SOFC (500–700 °C) based on doped ceria (DCO) electrolyte attracts much attention during the last decade since it allows stainless steel as interconnect, versatile sealant and improved long-term reliability [1].

Among the DCO oxides, Sm or Gd doped ceria has been extensively investigated and certified to possess the highest conductivity at comparative temperatures [2]. However, it suffers from electronic conduction caused by reduction reaction of Ce(IV) to Ce(III), resulting in lower open circuit voltages and output [3]. In addition, the specific grain-boundary conductivity was found to be between 2 and 7 orders of magnitude lower than the bulk conductivity [4]. So grain-boundary conductivity always plays a predominant role in the conduction process of doped ceria. In order to further improve the electrical properties of singly doped ceria, co-doping approach has been widely investigated and confirmed to be effective. Previous research has shown that the following advantageous factors can be benefited from co-doping, such as decrease of defect association enthalpy [5], increase of configurational entropy and pre-exponential factor of activation energy [6], improvement of elastic strain in the lattice [7], scavenging of impurity phases in the grain boundaries [8] and enhanced chemical stability to reduction [9], all of which can lead to the remarkably enhanced ionic conductivity over singly doped ceria.

From the standpoint of materials' cost, alkaline earth elements are more economically viable and readily available as codopants than rare earth elements. Moreover, the most distinguished feature of employing alkaline earth elements as codopants involves scavenging the highly resistive siliceous impurity phase in the grain boundaries, which greatly facilitates the grain-boundary conduction. Previous research has shown that MgO, CaO, SrO and BaO are effective to scavenge the siliceous impurity phase in the grain boundaries of Gd doped ceria (GDC) [8,10–12]. Co-doping ceria with alkaline earth and rare earth ion has also been certified to possess higher conductivity and lower activation energy than singly doped ceria [13–17].

Sr^{2+} is a cost-effective alkaline earth ion, in addition, the ionic radius of Sr^{2+} (1.25 Å) is relatively larger than that of Ce^{4+} (0.97 Å) in a VIII coordination. It is anticipated that the ionic conductivity will be enhanced by incorporation of Sr^{2+} ion since the microstructure of space charge layer near grain boundary might be optimized.

* Corresponding authors at: Division of Ceramic Technology, Department of Materials Science and Engineering, KTH Royal Institute of Technology, SE-10044 Stockholm, Sweden. Tel.: +46 08 7908324; fax: +46 08 207681.
E-mail addresses: zhangao@kth.se (Z. Gao), zhezhao@kth.se (Z. Zhao).

0378-7753/$ – see front matter © 2012 Elsevier B.V. All rights reserved.
doi:10.1016/j.jpowsour.2012.01.001

In this work, Sr is chosen as codopant for the host compound $Ce_{0.8}Sm_{0.2}O_{1.9}$, and the microstructures together with electrical properties have been investigated. The enhancement mechanism of ionic conductivity has also been discussed.

2. Experimental

Series of Sm and Sr co-doped ceria powders with formula of $Ce_{0.8}(Sm_{1-x}Sr_x)_{0.2}O_{2-\delta}$($x$ = 0, 0.3, 0.5, 0.7) was synthesized by a polyvinyl alcohol (PVA)-assisted sol–gel method. PVA (VWR International Ltd., Sweden) was dissolved in distilled water to obtain 5 wt.% PVA solution under heating and stirring. Stoichiometric $Ce(NO_3)_3{\cdot}6H_2O$ (99.9%, Alfa Aesar), $Sm(NO_3)_3{\cdot}6H_2O$ (99.9%, Alfa Aesar), $SrCO_3$(99.9%, Alfa Aesar) were dissolved in the diluted nitric acid, followed by addition of PVA solution as chelating agent. The mole ratio of —OH in the PVA to the metal cations was controlled to be 1:1. The pH value of the solution was adjusted to be around 7 using diluted ammonia solution. The obtained solution was heated to evaporate the excess water on a hot plate at 80 °C. A viscous and transparent sol formed, which was solidified by pre-annealing at 250 °C for 6 h in a muffle furnace. The obtained precursor powder was finally annealed at 600 °C for 2 h to eliminate the residence carbon and form well crystalline.

The powders were die-pressed into pellets with 13 mm in diameter and 1 mm in thickness under a pressure of 200 MPa. Subsequently, the green compact pellets were sintered at 1600 °C for 8 h to ensure the relative densities of all the final pellets to be higher than 98%, which was determined by the Archimedes method. Au paste was brushed on both surfaces of the pellet, followed by annealing at 800 °C for 30 min. A.C. impedance spectroscopy (SI 1260 Solartron Impedance/Gain-Phase Analyzer) was performed in air from 700 °C to 200 °C, in a frequency range of 100 mHz to 10 MHz using an excitation voltage of 10 mV under open circuit voltage (OCV) state. The sintered pellet with nominal composition of $Ce_{0.8}(Sm_{0.3}Sr_{0.7})_{0.2}O_{2-\delta}$ was polished and thermally etched at 1450 °C for 1 h for the morphology characterization.

The phase structure was characterized by the XRD with a PANalytical X'pert Pro diffractometer with monochromotized Cu Kα radiation at a 2θ scan rate of 2° min^{-1}. The morphology and microstructure of the powders and the pellets was performed by scanning electron microscope (SEM, JSM-7000F, JEOL Ltd., Japan) and transmission electron microscope (TEM, JEOL 2100LaB6).

3. Results and discussions

3.1. Microstructure

Fig. 1 shows the XRD patterns for the different samples after annealing at 600 °C. The broadened Bragg peaks indicate the nanocrystalline nature of the synthesized powder. All the samples are characterized with single phase, which can be well indexed by the cubic fluorite structure (JCPDS Card Number 04-0593). The crystallize size is calculated from the three main diffraction peaks by Scherrer's formula:

$$D = \frac{0.9\lambda}{\beta \cos\theta} \quad (1)$$

where D is the crystallize size (nm), λ is the X-ray wavelength (0.15406 nm for Cu target), 2θ is the diffraction angle, and β is the full-width at half-maximum of peaks. The sizes of the particles are 15.3 nm, 14.5 nm, 15.4 nm, 17.6 nm according to the calculations.

Fig. 2 presents the TEM images of the nanocrystalline $Ce_{0.8}(Sm_{0.7}Sr_{0.3})_{0.2}O_{2-\delta}$ powder. As shown in Fig. 2a, the particle size is about 5–20 nm with irregular shape, which agrees well with the XRD results. The particles form agglomeration due to the high surface energy during the synthesis process. The crystal

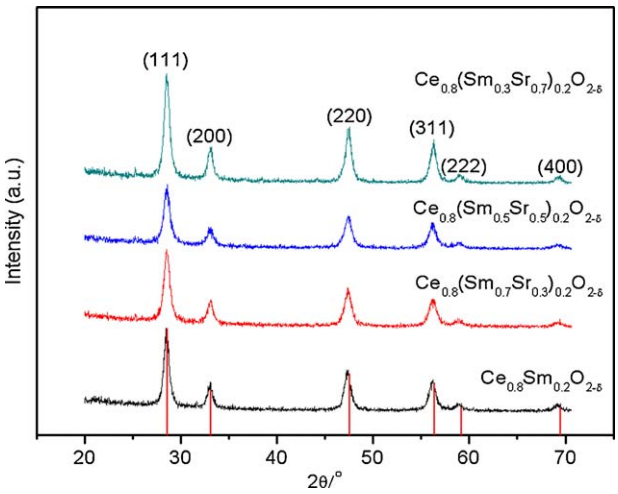

Fig. 1. XRD patterns for the different samples after being sintered at 600 °C for 2 h. The standard is JCPDS powder diffraction file no. 04-0593.

plane fringe can be clearly seen in Fig. 2b, indicating the powder sample has crystallized well. The distance between adjacent fringes is approximately 0.273 nm, which is close to the d-spacing of the (2 0 0) plane of the CeO_2 standard (0.2706 nm).

As shown in Fig. 3a, the $Ce_{0.8}(Sm_{0.7}Sr_{0.3})_{0.2}O_{2-\delta}$ powder appears flake-like foam morphology. The flake-like morphology is mainly caused by the PVA, since the PVA is linear structure and acts as chelating agent during the powder synthesis process. Fig. 3b and c presents the cross-section view and surface micrograph of the pellet with the nominal composition of $Ce_{0.8}(Sm_{0.3}Sr_{0.7})_{0.2}O_{2-\delta}$ after being sintered at 1600 °C. The pellet displays dense structure from

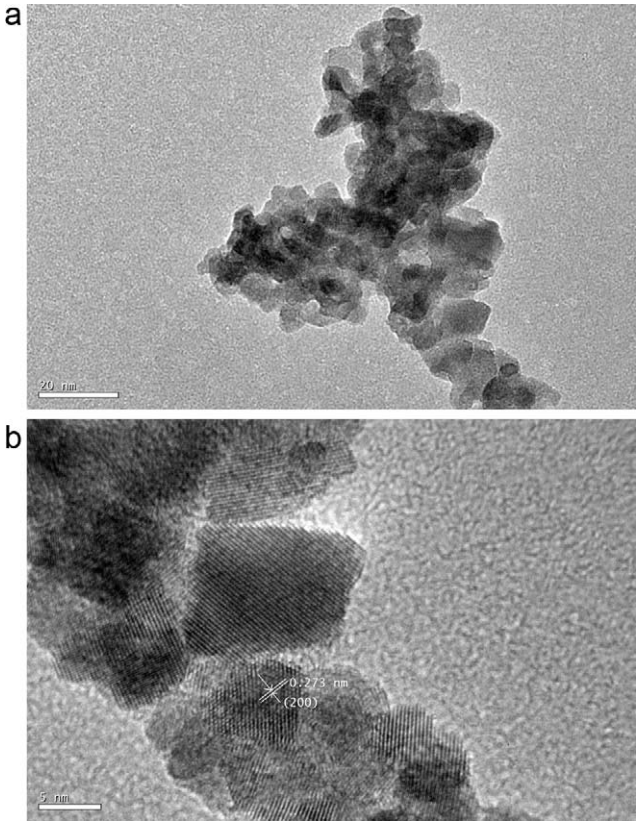

Fig. 2. (a) TEM images for the nanocrystalline $Ce_{0.8}(Sm_{0.7}Sr_{0.3})_{0.2}O_{2-\delta}$ powder and (b) HRTEM image of $Ce_{0.8}(Sm_{0.7}Sr_{0.3})_{0.2}O_{2-\delta}$ powder.

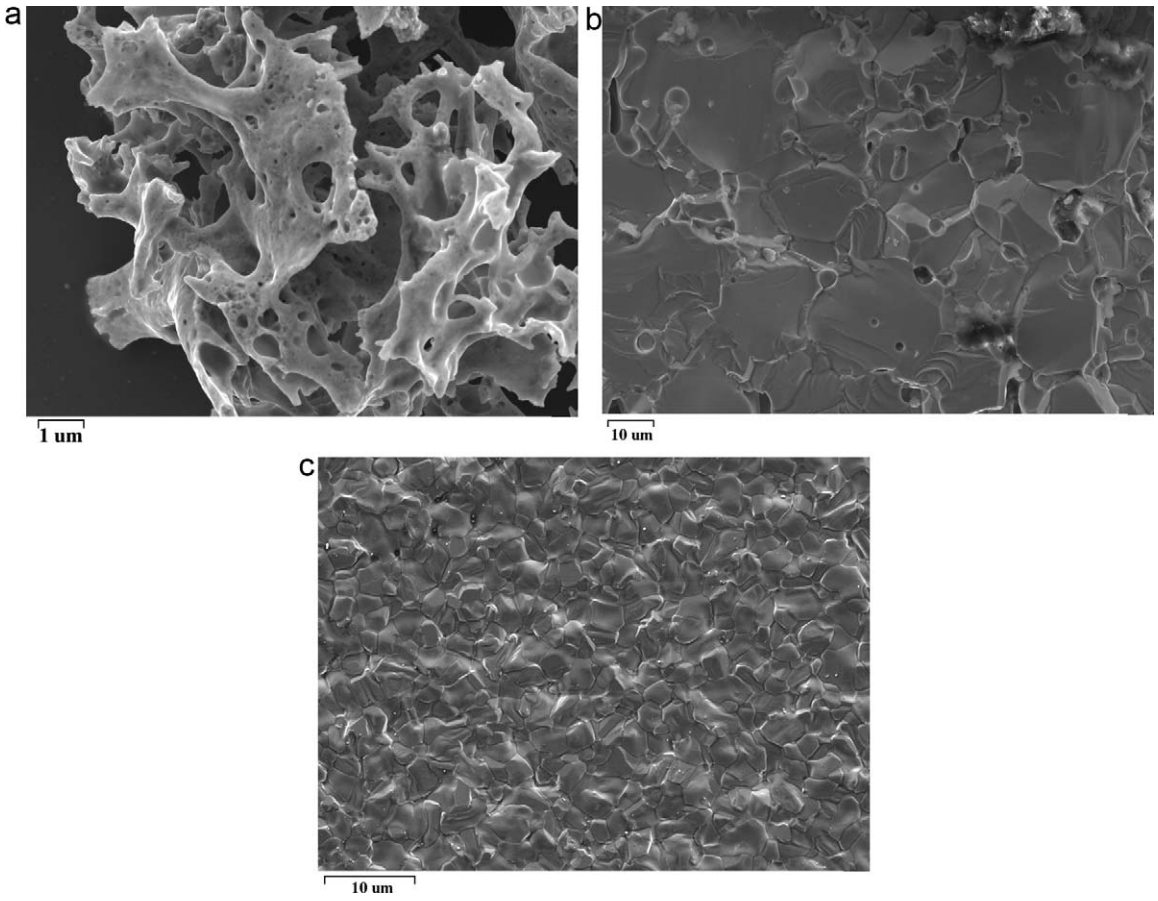

Fig. 3. SEM images for (a) $Ce_{0.8}(Sm_{0.7}Sr_{0.3})_{0.2}O_{2-\delta}$ powder, (b) cross-section view for the $Ce_{0.8}(Sm_{0.3}Sr_{0.7})_{0.2}O_{2-\delta}$ pellet, (c) surface view for the $Ce_{0.8}(Sm_{0.3}Sr_{0.7})_{0.2}O_{2-\delta}$ pellet after thermally etching.

the surface micrograph; however, there are still some pores in the sample from the cross-section micrograph. It can be true that the simple ceramic processing procedure taken in the present study is not perfect for fully densification, but this will not induce any effect on the co-doping effect investigated here due to the very similar density and microstructure between different samples. The well-defined grains separated by the grain boundaries have been clearly detected in Fig. 3c. The average grain size of the etched sample is 3.3 μm, which is obtained by using the linear intercept technique [18].

3.2. A.C. impedance spectra

Fig. 4 shows the typical impedance spectra for different samples measured at 300 °C. Three contributions can be detected from the plots. The high-frequency arc can be ascribed to the bulk polarization; the intermediate-frequency arc and the low-frequency arc are designated to the grain-boundary polarization and electrode polarization, respectively. The contributions of bulk resistances and grain-boundary resistances to total resistances can be resolved by different relaxation times or capacitances in the impedance spectra. Ideally, the frequency response of polycrystalline doped ceria can be modeled by a resistor and a lossy capacitor (RC) in parallel. The capacitance can be calculated by using Eq. (2) [19]:

$$C_i = \frac{1}{\omega_{\max} R_i} \tag{2}$$

where C_i is the bulk or the grain-boundary capacitance; R_i is the bulk or the grain-boundary resistance; $\omega_{\max}$ is the frequency of maximum loss in the impedance spectrum.

However, in our case, taking the microstructure inhomogeneity of the samples into account, the lossy capacitor has been replaced by a constant phase element (CPE). The impedance spectra have been modeled by the Zview software using the configuration of $(R_1\mathrm{CPE}_1)(R_2\mathrm{CPE}_2)(R_3\mathrm{CPE}_3)$, where R_1 (R_b) is the bulk resistance, R_2 (R_{gb}) is the grain-boundary resistance, R_3 (R_e) is electrode resistance.

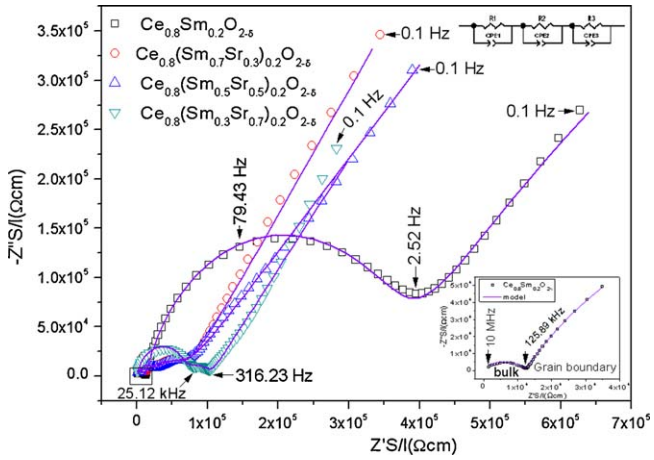

Fig. 4. Typical impedance spectra for different samples measured at 300 °C; insert is the equivalent circuit employed to fit the impedance spectra; the solid lines are fitting curves.

The capacitance can be calculated from Eq. (3) [20]:

$$C_i = \frac{(R_i Q_i)^{1/n}}{R_i} \quad (3)$$

where Q_i is the pseudocapacitance and n is the similarity between the CPE and real capacitor, for which $n = 1$.

The capacitance values originated from Eqs. (2) and (3) are presented in Table 1. The results from Eq. (3) are one order of magnitude lower than the results from Eq. (2). The values from Eq. (3) are in the range of $3–7 \times 10^{-11}$ F for bulk capacitance, and $2–70 \times 10^{-9}$ F for grain-boundary capacitance, which are quite similar with the previous results [5]. Additionally, as shown in Fig. 4, the fitted curves can perfectly match the measured results. It indicates that the results originated from Eq. (3) are more reliable than those from Eq. (2) and the obtained bulk and grain-boundary resistances are quite reasonable. It is difficult to differentiate the grain-boundary resistance and the bulk resistance above 500 °C since the contribution from bulk resistance could not be observed. Previous research from Perez-Coll et al. indicates that the grain-boundary conduction shows a linear behavior in the Arrhenius equation [21]. We reasonably assume that the Arrhenius relationship of the reciprocal of grain-boundary resistances with respect to the reciprocal of temperatures is linear. The bulk resistance can be obtained from the difference of the total resistance and the extrapolated grain-boundary resistance. In some cases, the equivalent circuit fitting is also utilized to obtain the bulk and grain-boundary resistance when the temperature is higher than 500 °C. The grain-boundary resistances are observed to decrease whereas the bulk resistances increase with the Sr addition content.

3.3. Conductivities

The total resistance (R_t) of the electrolyte can be expressed as the sum of bulk resistance (R_b) and grain-boundary resistance (R_{gb}):

$$R_t = R_b + R_{gb} \quad (4)$$

The conductivities can be calculated by the following formula:

$$\sigma_i = \frac{L}{SR_i} \quad (5)$$

where L is the sample thickness, S is the electrode active area. Contribution from electronic conductivity is assumed to be negligible to the total conductivity since reduction reaction of Ce(IV) to Ce(III) can only occur at high temperatures (>1000 °C) and low oxygen pressures [22], in addition, all of our measurements are executed at temperatures lower than 700 °C in air. Therefore, in this work, all the mentioned conductivity is designated to the ionic conductivity.

Fig. 5 presents the Arrhenius plots of bulk conductivities, grain-boundary conductivities, specific grain-boundary conductivities and total conductivities. As shown in Fig. 5a, the bulk conductivities first increase with increasing Sr addition content up to $x = 0.3$. The introduction of divalent and trivalent elements into the ceria creates oxygen vacancy and they are responsible for the ionic conduction. The oxygen vacancy creation can be written using Kröger–Vinker notation.

$$SrO = Sr''_{Ce} + V_O^{\bullet\bullet} + O_O^x \quad (6)$$

$$Sm_2O_3 = 2Sm'_{Ce} + V_O^{\bullet\bullet} + 3O_o^x \quad (7)$$

$$O_o^x + 2Ce_{Ce}^x = 1/2O_2(gas) + V_O^{\bullet\bullet} + 2Ce'_{Ce} \quad (8)$$

where Sm'_{Ce} and Sr''_{Ce} indicates the Ce^{4+} site has been occupied by Sm^{3+} and Sr^{2+}, respectively, producing the negative charges. Consequently, the oxygen vacancies are created according to the charge compensation mechanism. The enhancement in bulk conductivities can be mainly ascribed to the increased number of oxygen

Table 1
Capacitance values originated from different calculations at 300 °C.

	$Ce_{0.8}Sm_{0.2}O_{2-\delta}$		$Ce_{0.8}(Sm_{0.7}Sr_{0.3})_{0.2}O_{2-\delta}$		$Ce_{0.8}(Sm_{0.5}Sr_{0.5})_{0.2}O_{2-\delta}$		$Ce_{0.8}(Sm_{0.3}Sr_{0.7})_{0.2}O_{2-\delta}$	
	Bulk	Grain boundary	Bulk	Grain boundary	Bulk	Grain boundary	Bulk	Grain boundary
$C_i = \frac{1}{\omega_{max} R_i}$ (F)	2.9852×10^{-10}	4.4357×10^{-7}	2.4013×10^{-10}	3.6876×10^{-8}	1.5132×10^{-10}	1.8136×10^{-8}	1.7609×10^{-10}	3.3155×10^{-8}
$C_i = \frac{(R_i Q_i)^{1/n}}{R_i}$ (F)	4.2474×10^{-11}	6.8040×10^{-8}	6.7425×10^{-11}	2.0933×10^{-9}	4.1599×10^{-11}	2.7497×10^{-9}	3.1521×10^{-11}	5.8995×10^{-9}

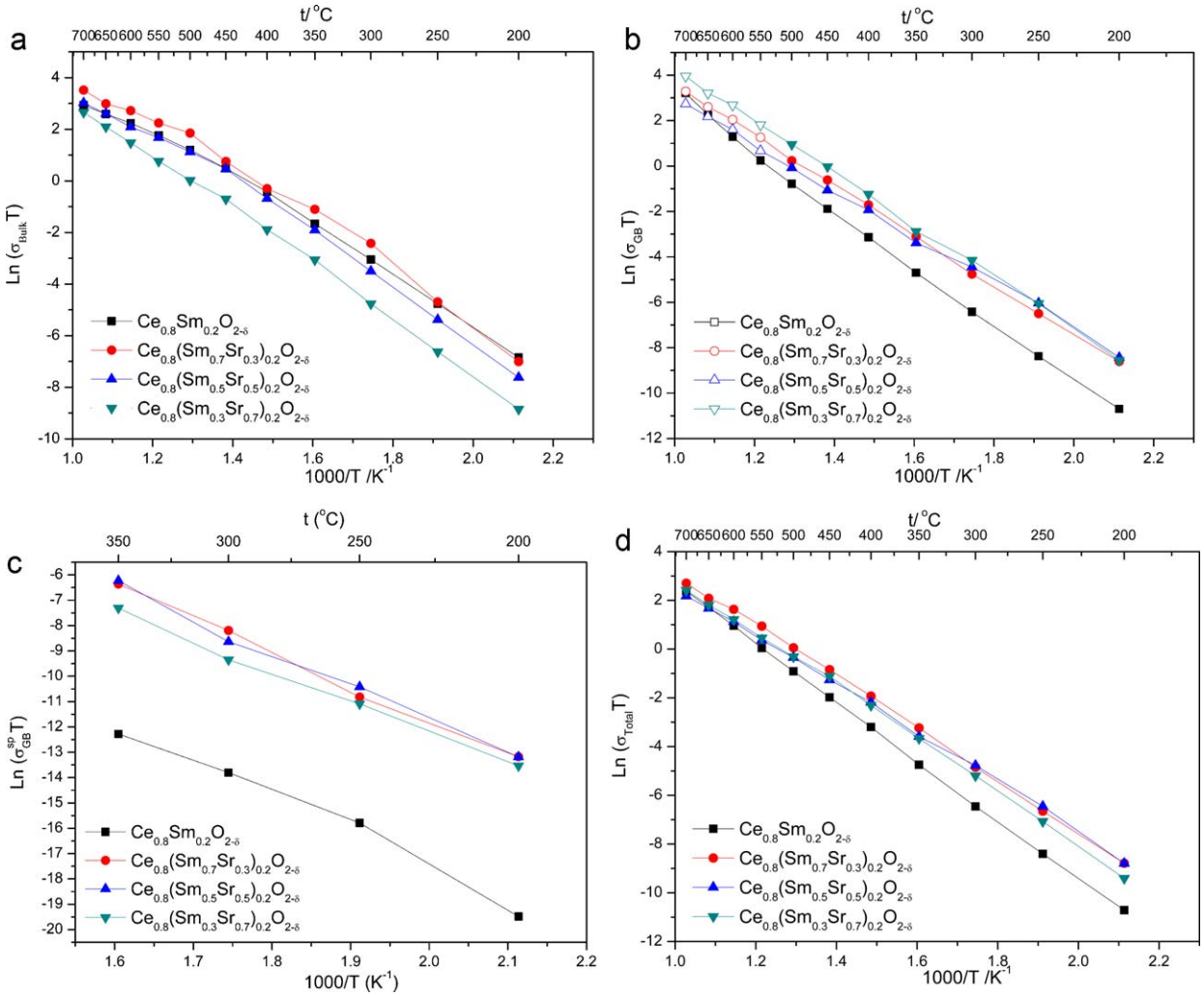

Fig. 5. Arrhenius plots of (a) bulk conductivities, (b) grain-boundary conductivities, in which the extrapolated data appear as hollow symbols, (c) specific grain-boundary conductivities, (d) total conductivities for different samples.

vacancies caused by the Sr substitution. Moreover, the Sr addition suppresses the ordering of oxygen vacancies, optimizing the distribution of oxygen vacancies and leading to the increase in the bulk conductivities [23]. A further increase in the Sr addition content will lead to reduced bulk conductivities. This phenomenon can be probably due to the immobile clusters, resulting in the reduction of free oxygen vacancies. The elastic strain also increases in the lattice resulting from the substantial ion size mismatch between Sr^{2+} dopant and Ce^{4+} host cation [7]. Furthermore, the more intense defect association is assumed to occur with the increased Sr^{2+}/Sm^{3+} ratio. The positive vacancy $V_O^{\bullet\bullet}$ may attract the negative Sm'_{Ce} and Sr''_{Ce} doping ions, forming $Sm'_{Ce}\,V_O^{\bullet\bullet}$/$Sm'_{Ce}\,V_O^{\bullet\bullet}\,Sm'_{Ce}$, $Sr''_{Ce}\,V_O^{\bullet\bullet}$ or $Sr''_{Ce}\,V_O^{\bullet\bullet}\,Sr''_{Ce}$ due to the electrostatic attraction [24]. All these associate state can decrease the mobile oxygen vacancy concentration, leading to the decrease in the bulk conductivities. In addition, due to the larger ionic radius, Sr^{2+} can even possess stronger electrostatic attraction force to the oxygen vacancy than Sm^{3+}. Consequently, more substantial defect associations can be expected, e.g. $Sr''_{Ce}\,V_O^{\bullet\bullet}$ or $Sr''_{Ce}\,V_O^{\bullet\bullet}\,Sr''_{Ce}$, resulting in much lower bulk conductivity than $Ce_{0.8}Sm_{0.2}O_{1.9}$.

The grain-boundary conductivities exhibit a continuous increment with the increasing Sr addition content, with the exception of $Ce_{0.8}(Sm_{0.5}Sr_{0.5})_{0.2}O_{2-\delta}$, as shown in Fig. 5b. The space charge theory has been proposed and utilized to elucidate the conduction behavior at grain boundaries [25]. In this theory, the grain-boundary core is positively charged due to the enrichment of oxygen vacancies, resulting in the depletion of oxygen vacancies in the space charge layer, which has significant effect on the electrical properties of doped ceria. The negative Sm'_{Ce} and Sr''_{Ce} interacts with the positive grain-boundary core of ceria due to the coulombic attraction force, resulting in the enrichment of Sm and Sr solute at the space charge layers.

The specific grain-boundary conductivity, which reflects the real geometry of the grain boundaries, can be obtained from Eq. (9) assuming the bulk and grain-boundary permittivity is similar [20].

$$\sigma_{GB}^{sp} = \left(\frac{C_b}{C_{GB}}\right)\sigma_{GB} \tag{9}$$

where σ_{GB}^{sp} is the specific grain-boundary conductivity; C_b is the bulk capacitance; C_{GB} is the grain-boundary capacitance and σ_{GB} is the grain-boundary conductivity. The capacitance can be calculated from Eq. (3).

Fig. 5c presents the specific grain-boundary conductivities of different specimens. The specific grain-boundary conductivities are observed to increase with the Sr addition content up to $x = 0.5$. It indicates that the Sr addition greatly alleviate the oxygen vacancy "depletion" state in the space charge layer, which is responsible for the enhancement of specific grain-boundary conductivities. Further increase in Sr addition content will lead to a decrease in specific grain-boundary conductivities, which can be

mainly ascribed to the formation of minor secondary phase containing SrO in grain boundaries, since the limit of Sr solubility into the CeO_2 has been reached. At 300 °C, the specific grain-boundary conductivities for $Ce_{0.8}(Sm_{1-x}Sr_x)_{0.2}O_{2-\delta}$ (x = 0, 0.3, 0.5, 0.7) are 1.77×10^{-9} S cm^{-1}, 4.83×10^{-7} S cm^{-1}, 3.10×10^{-7} S cm^{-1}, 1.52×10^{-7} S cm^{-1}, respectively, which are similar to the previous studies [20,21,26,27], where only small grained $Gd_{0.2}Ce_{0.8}O_{2-\delta}$ and $Dy_{0.2}Ce_{0.8}O_{2-\delta}$ sintered at low temperature show the specific grain boundary conductivity on the level of 10^{-7} S cm^{-1}. Considering the relatively high sintering temperature at 1600 °C and coarse grain size, the high specific grain boundary conductivities shown in all the Sm and Sr co-doped samples further indicate the reduced grain boundary "depletion" by present doping strategy. The total conductivities increase with the Sr addition content up to x = 0.3, reaching the maximum values, as shown in Fig. 5d. Further increase in Sr addition content will lead to a decrease in the total conductivities. Evidently, all the total conductivities of Sm and Sr codoped ceria are higher than those of $Ce_{0.8}Sm_{0.2}O_{1.9}$, indicating that co-doping at optimum concentration can effectively improve the conductivity of the singly doped ceria.

3.4. Activation energies

The obtained conductivities can be analyzed by using the Arrhenius equation:

$$\sigma T = A \ \exp\left(-\frac{E_a}{kT}\right) \tag{10}$$

where E_a is the activation energy of ion conduction, κ is Boltzman's constant, T is the absolute temperature, and A is the pre-exponential factor, which closely relates to the fraction of free oxygen vacancies and entropy change during migration of charged particles [28]. The activation energy (E_a) is the sum of the migration enthalpy (ΔH_m) and the association enthalpy (ΔH_a). Therefore, Eq. (10) can be transferred into Eq. (11):

$$\sigma T = A \ \exp\left(-\frac{\Delta H_m + \Delta H_a}{kT}\right) \tag{11}$$

ΔH_m is assumed to be independent of the temperature and dopant concentrations [29]. E_a is predominantly determined by ΔH_a. At high temperatures, E_a is only dependent on ΔH_m since all the defects are fully dissociated ($\Delta H_a \rightarrow 0$). There is a transition for defects from associated state to dissociated state in the Arrhenius plots. As shown in Fig. 5a, the significant bending of Arrhenius plots lie in the regime of 400–500 °C. ΔH_m and ΔH_a can be conceivably calculated according to Eq. (11) in the temperature range of 200–400 °C and 500–700 °C, respectively.

The activation energies derived from the Arrhenius plots of bulk conductivities for various samples are shown in Fig. 6a. The activation energies of bulk conductivities are observed to slightly increase with the increasing Sr addition content, which can be attributed to the larger lattice strain caused by the ionic radius mismatch of Sr^{2+} and Ce^{4+} [7]. ΔH_a exhibits the maximum value at x = 0.3. ΔH_m first decreases then increases with the increasing Sr addition content, exhibits a minimum value at x = 0.3. The migration enthalpy depends on the local atomic arrangement [30]. The decrease in ΔH_m can be mainly ascribed to the increase of vacancy concentration and the improved transportation paths [30] whereas the increase in ΔH_m can be attributed to the reduction of free oxygen vacancies caused by the immobile clusters and the formation of locally ordered oxygen vacancy clusters or microdomains near grain boundaries [31]. The pre-exponential factor first increases with the Sr addition content up to x = 0.3, which is closely related to the higher oxygen vacancy concentration by substituting Sm with Sr. Such an increase in pre-exponential factor, which is always interpreted as the number of effective oxygen vacancy, agrees very well with the change in the bulk conductivity. A further increase in the Sr addition content leads to a decrease of the pre-exponential factor. This probably indicates that higher dopant of Sr leads to more associated oxygen vacancy clusters even more oxygen vacancies have been generated. From Eq. (10), we can see that the bulk conductivity is determined by both the pre-exponential factor and the activation energy. Though there is a slight increase in the activation energy, the improvement of pre-exponential factor can compensate for this effect.

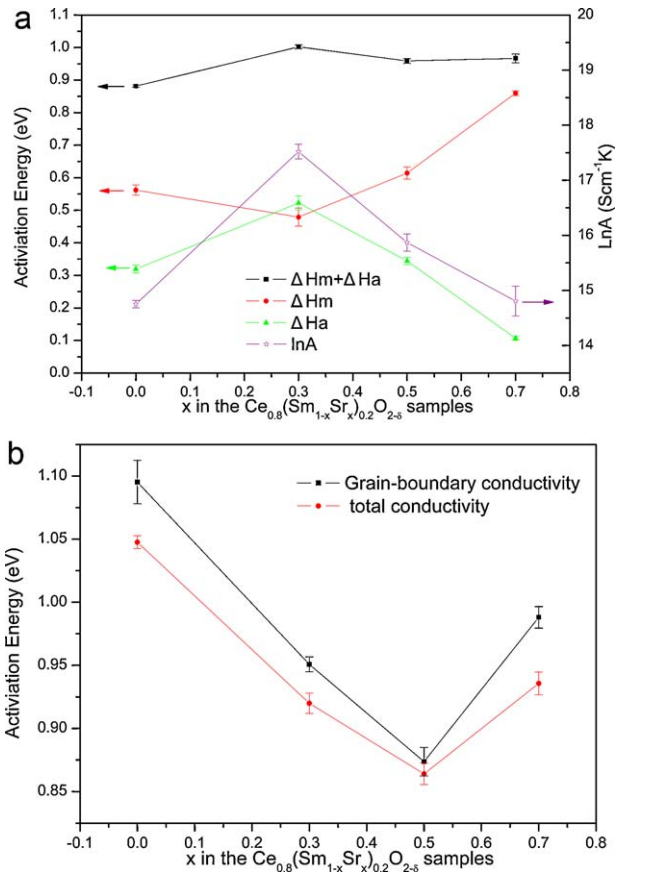

Fig. 6. (a) activation energy, migration enthalpy, defect association enthalpy and ln$A$ of the grain as a function of Sr addition content; and (b) activation energy of grain-boundary conductivity and total conductivity as a function of Sr addition content.

As shown in Fig. 6b, The activation energies of grain-boundary conductivities first decrease with the addition of Sr addition content up to x = 0.5, which can be ascribed to the alleviated oxygen vacancy "depletion" state in space charge layers at the grain boundaries. However, the activation energies will increase with further increasing Sr addition content. Evidently, this behavior is contradicted with the variation trend of grain-boundary conductivities as shown in Fig. 5b, where the grain-boundary conductivities show a continuous increment, except for minor deviation with $Ce_{0.8}(Sm_{0.5}Sr_{0.5})_{0.2}O_{2-\delta}$. Similar to the analysis for the bulk conductivity, this phenomenon with grain boundary-conductivity should be the comprehensive effect of the increased oxygen vacancy number and the increased oxygen vacancy clusters. The activation energies of total conductivities yield the minimum value when x = 0.5. This agrees well with the change in the activation energies of grain-boundary conductivities. Additionally, the activation energies of grain-boundary conductivities are higher than those of the bulk conductivities, indicating the activation energies of grain-boundary conductivities are predominant which determines the total conductivities.

4. Conclusions

Sr addition has been executed with the aim of enhancing the ionic conductivity of $Ce_{0.8}Sm_{0.2}O_{2-\delta}$. The effect of Sr addition content on the bulk conductivities, grain-boundary conductivities and total conductivities of the doped ceria has been investigated and the mechanism has been discussed. The $Ce_{0.8}(Sm_{0.7}Sr_{0.3})_{0.2}O_{2-\delta}$ exhibits the highest bulk conductivities among all series. The apparent grain-boundary conductivities increase with increasing Sr concentration, except for the minor deviation with $Ce_{0.8}(Sm_{0.5}Sr_{0.5})_{0.2}O_{2-\delta}$. The specific grain-boundary conductivities reach maximum for $x = 0.5$. The results show that the Sr addition not only increase the effective charge carriers for bulk conductivity, but also greatly alleviate the oxygen vacancy "depletion" state in space charge layers. The total conductivities of all Sm and Sr co-doped ceria are higher than that of $Ce_{0.8}Sm_{0.2}O_{1.9}$. The results indicate that co-doping with Sm and Sr at optimum content can effectively improve the ionic conductivity of the Sm doped ceria.

Acknowledgement

The authors gratefully acknowledge the financial support from Wallenberg Foundation for the electron microscopy measurement in Arrhenius laboratory, Stockholm University.

References

[1] B.C.H. Steele, A. Heinzel, Nature 414 (2001) 345–352.
[2] B.C.H. Steele, Solid State Ionics 129 (2000) 95–110.
[3] X.G. Zhang, M. Robertson, S. Yick, C. Deces-Petit, E. Styles, W. Qu, Y.S. Xie, R. Hui, J. Roller, O. Kesler, R. Maric, D. Ghosh, J. Power Sources 160 (2006) 1211–1216.
[4] X. Guo, W. Sigle, J. Maier, J. Am. Ceram. Soc. 86 (2003) 77–87.
[5] W. Zajac, J. Molenda, Solid State Ionics 179 (2008) 154–158.
[6] B. Li, Y.Y. Liu, X. Wei, W. Pan, J. Power Sources 195 (2010) 969–976.
[7] S. Omar, E.D. Wachsman, J.C. Nino, Solid State Ionics 177 (2006) 3199–3203.
[8] P.S. Cho, Y.H. Cho, S.Y. Park, S.B. Lee, D.Y. Kim, H.M. Park, G. Auchterlonie, J. Drennan, J.H. Lee, J. Electrochem. Soc. 156 (2009) B339–B344.
[9] S. Banerjee, P.S. Devi, D. Topwal, S. Mandal, K. Menon, Adv. Funct. Mater. 17 (2007) 2847–2854.
[10] P.S. Cho, S.B. Lee, Y.H. Cho, D.Y. Kim, H.M. Park, J.H. Lee, J. Power Sources 183 (2008) 518–523.
[11] S.Y. Park, P.S. Cho, S.B. Lee, H.M. Park, J.H. Lee, J. Electrochem. Soc. 156 (2009) B891–B896.
[12] Y.H. Cho, P.S. Cho, G. Auchterlonie, D.K. Kim, J.H. Lee, D.Y. Kim, H.M. Park, J. Drennan, Acta Mater. 55 (2007) 4807–4815.
[13] Y.F. Zheng, H.T. Gu, H. Chen, L. Gao, X.F. Zhu, L.C. Guo, Mater. Res. Bull. 44 (2009) 775–779.
[14] N. Cioatera, V. Parvulescu, A. Rolle, R.N. Vannier, Solid State Ionics 180 (2009) 681–687.
[15] S. Ramesh, V.P. Kumar, P. Kistaiah, C.V. Reddy, Solid State Ionics 181 (2010) 86–91.
[16] Y.F. Zheng, L.Q. Wu, H.T. Gu, L. Gao, H. Chen, L.C. Guo, J. Alloys Compd. 486 (2009) 586–589.
[17] M. Dudek, A. Rapacz-Kmita, M. Mroczkowska, M. Mosialek, G. Mordarski, Electrochim. Acta 55 (2010) 4387–4394.
[18] Y.R. Wang, T. Mori, J.G. Li, J. Drennan, J. Eur. Ceram. Soc. 25 (2005) 949–956.
[19] J.T.S. Irvine, D.C. Sinclair, A.R. West, Adv. Mater. 2 (1990) 132–138.
[20] C. Sanchez-Bautista, A.J. Dos Santos-Garcia, J. Pena-Martinez, J. Canales-Vazquez., Solid State Ionics 181 (2010) 1665–1673.
[21] D. Perez-Coll, D. Marrero-Lopez, P. Nunez, S. Pinol, J.R. Frade, Electrochim. Acta 51 (2006) 6463–6469.
[22] G.B. Balazs, R.S. Glass, Solid State Ionics 76 (1995) 155–162.
[23] H. Yamamura, E. Katoh, M. Ichikawa, K. Kakinuma, T. Mori, H. Haneda, Electrochemistry 68 (2000) 455–459.
[24] L.P. Li, G.S. Li, J. Xiang, R.L. Smith, H. Inomata, Chem. Mater. 15 (2003) 889–898.
[25] X. Guo, R. Waser, Prog. Mater. Sci. 51 (2006) 151–210.
[26] D. Perez-Coll, P. Nunez, J.R. Frade, J.C.C. Abrantes, Electrochim. Acta 48 (2003) 1551–1557.
[27] D. Perez-Coll, P. Nunez, J.C. Ruiz-Morales, J. Pena-Martinez, J.R. Frade, Electrochim. Acta 52 (2007) 2001–2008.
[28] E.Y. Pikalova, A.A. Murashkina, V.I. Maragou, A.K. Demin, V.N. Strekalovsky, P.E. Tsiakaras, Int. J. Hydrogen Energy 36 (2011) 6175–6183.
[29] I.E.L. Stephens, J.A. Kilner, Solid State Ionics 177 (2006) 669–676.
[30] D.A. Andersson, S.I. Simak, N.V. Skorodumova, I.A. Abrikosov, B. Johansson, Proc. Natl. Acad. Sci. U. S. A. 103 (2006) 3518–3521.
[31] T. Mori, R. Buchanan, D.R. Ou, F. Ye, T. Kobayashi, J.D. Kim, J. Zou, J. Drennan, J. Solid State Electrochem. 12 (2008) 841–849.